Aerodynamic Performance of an Arrow Airfoil in Mars Environment and its Optimization

Soonmoung Kwon[1], Yoonpyo Hong[1], Kwanjung Yee[1*]

[1*]Dept. Of Aerospace Engineering
Seoul National University, Seoul, 08826, Republic of Korea
ksm960515@snu.ac.kr / hyp1227@snu.ac.kr / kjyee@snu.ac.kr

Abstract

A novel arrow airfoil is proposed in the Mars atmospheric condition for high $\mathrm{L/D}$, and the flow characteristics around the airfoil are investigated through numerical analysis. Since the bubble on the upper surface of the airfoil by the arrow, the lift increased and the frictional drag decreased, in turn, $\mathrm{L/D}$ increases. The optimized arrow airfoil that maximizes the maximum $\mathrm{L/D}$ over angle of attack 0 to 10° is obtained under the operating condition of NASA Mars Helicopter Technology Demonstrator(MHTD), based on 5% cambered flat plate airfoil. There is an increase in maximum $\mathrm{L/D}$ of 10.51% and 7.05% in the first and second flow conditions, respectively, and no design is derived that satisfies the constraints in the third flow condition. In addition, off-design analysis of optimum arrow airfoil is conducted to investigate the effect of Mach number, and it is confirmed that arrow airfoil is effective at $\mathrm{M} = 0.5$ or less.

1. INTRODUCTION

Interest in small UAV-based exploration that will fill the gap between satellite exploration and rover-based exploration is growing in Mars exploration. Among the exploration methods currently being carried out, rover-based exploration has a high resolution of information, but its scope is limited. Although satellite exploration has a wide range, it has a disadvantage in that the resolution of information is low. Small UAV-based exploration is expected to play an important role in Mars exploration by complementing the shortcomings of each of the rover-based exploration and satellite exploration, and also have a significant impact on manned exploration. In particular, research on vertical take-off and landing aircraft, which is not affected by the rough surface of Mars and has advantages of hovering and landing, is being actively conducted. On Mars, however, UAV operates in a thin Martian atmosphere, about 1% of Earth, and low speed of sound due to the carbon-dioxide-based atmosphere. In other words, it is operated in a region with a relatively high Mach number and a low Reynolds number compared to the earth, so that the lift is low and the drag is increased, resulting in poor aerodynamic performance. To overcome the above problems, an in-depth design of the rotor system is required. As the operating conditions are completely different, the airfoil design is the most important among the rotor systems.

Many studies have been conducted on the flow phenomenon that appears in low Reynolds number flow and airfoil design on that condition. The characteristics of the laminar separation bubble near the leading edge, transition, and turbulence reattachment in low Reynolds number flows were studied by Arena[1], O'Meara[2], and Sunada[3]. Munday[4] revealed through experiments and numerical analysis that, in the low Reynolds number flow of a triangular airfoil, the lift increases due to the laminar separation bubble and leading-edge vortex, resulting in a non-linear lift increment. In low Reynolds number flow, the effect of viscosity is greater than inertia because the flow remains laminar upstream of the airfoil. Therefore, flow separation occurs easily due to the lower energy of flow to overcome the adverse pressure gradient, and then, as the flow transitions to turbulence, it reattaches to form a laminar separation bubble. Because the pressure inside the laminar separation bubble is low, the lift increases. The laminar separation bubble is a very complicated phenomenon because it is a problem of transition, and it is difficult to predict because the separation point keeps changing according to the Reynolds number. However, it has been shown that to predict the complex phenomena appearing in low Reynolds number flows such as the locations of separation and reattachment points, and transitions and aerodynamic performance such as lift coefficient are possible based on 2D and 3D RANS analysis by Lee[5],[6].

Presented at 47th European Rotorcraft Forum, United Kingdom, 7-9th September, 2021

In the view of the design of airfoil, Schmitz [7], [8] presented three shape characteristics of an efficient airfoil at a low Reynolds number. 1) The Reynolds number dependency is reduced by fixing the separation point with a sharp leading edge. 2) The flat upper surface reduces the separation region. 3) Camber makes the lift increase. 1) and 3) can be applied to the current design, but in the case of 2), it is not correct because the lift increase due to separation and resulting separation bubble is an important factor. Liebeck[9] studied the characteristics of low Reynolds number flow and airfoil design accordingly, but it did not deviate from the smooth airfoil. Oyama[10] parameterized the airfoil using a B-Spline curve using six control points excluding the leading and trailing edges, based on the conceptual design of the Mars UAV presented by Tanaka[11] and using a genetic algorithm to optimized airfoil which has the best $\mathrm{L/D}$ at an angle of attack 2° at the Reynolds number 100,000 (Mars condition) or 10,000,000 (Earth condition), and Mach numbers 0.48 and 0.65. As a result, it was confirmed that the airfoil optimized for Mars conditions is thinner than the airfoil optimized for Earth conditions and the camber is larger. The study revealed that the thinner the airfoil, the higher the $\mathrm{L/D}$, and the camber must be applied to compress the air at the bottom and expand the air at the top of the airfoil. However, it was pointed out that if the camber is too large, separation occurs and the $\mathrm{L/D}$ decreases. Also, the optimized airfoil was structurally impossible with a maximum thickness of less than 0.002 of the chord length, and the parameterization method was also limited to implement an airfoil with a complex shape. The NACA 4-digit airfoil was optimized for Mars rotorcraft by Zhao[12], but there was a limit to the shape that could be expressed. Koning[13][14][15][16] studied the airfoil to be used in the rotor system of NASA Mars Helicopter Technology Demonstrator(MHTD), and evaluated the performance of 5% cambered plate at a low Reynolds number, and compared the airfoil of MHTD. Based on previous studies, the types of the airfoil that can be used on Mars were classified into four types. And based on this, a different parameterization method was proposed for each type. It was discovered that separation from the leading edge, and creating and maintaining a bubble through it, increase the $\mathrm{L/D}$ of the airfoil. However, the presented parameterization method is not focused on bubble formation, so there is a limit to create and control the bubble.

Through previous studies, the flow characteristics and the effects of low Reynolds number were revealed. And from several optimization results, features for efficient airfoil design at low Reynolds number were presented. In particular, it has been found that the separation bubble increases lift, thereby increasing $\mathrm{L/D}$. However, the design of the airfoil focused on the effect of the separation bubble has not been much studied.

In this study, a new type of airfoil, arrow airfoil, is proposed for Mars rotorcraft, to increase the $\mathrm{L/D}$ by creating and controlling bubbles by adding a notch at the leading edge of the 5% cambered plate airfoil. And the flow characteristics around the airfoil are investigated through numerical analysis, and the performance is compared with that of a 5% cambered plate airfoil. The optimized arrow airfoil that maximizes the maximum L/D over an angle of attack 0 to 10° is obtained using the surrogate model and genetic algorithm. In addition, off-design analysis of optimum arrow airfoil is conducted to investigate the effect of Mach number.

The physical characteristics of the arrow airfoil are presented in section 2. In section 3, the method of numerical analysis and the flow conditions are described. Also, the parameterization method of the arrow, surrogate modeling, and optimization method are shown. The optimized airfoil of each flow condition is analyzed and the effect of the Mach number is discussed in section 4. Finally, summarize of this research is shown in section 5.

2. ARROW AIRFOIL

In this section, the arrow airfoil is briefly described and the performance of the arrow airfoil is compared with the baseline airfoil. A 5% cambered flat plate airfoil that has a thickness of 1% of the chord length and a cambered of 5% of the chord length is depicted in Fig 1. The thickness increases linearly from the leading edge to 0.1 chord length. The 5% cambered flat plate is known to have high $\mathrm{L/D}$ in low Reynolds number flow, so it is used as a baseline airfoil. Figure 2 shows an optimum arrow airfoil at the flow conditions of $\mathrm{Re} = 11{,}912$ and $\mathrm{M} = 0.3116$.

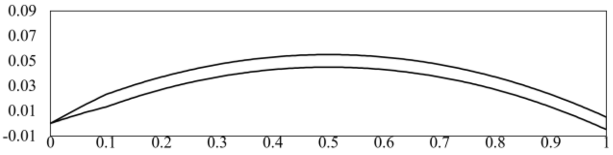

Figure 1 Baseline airfoil

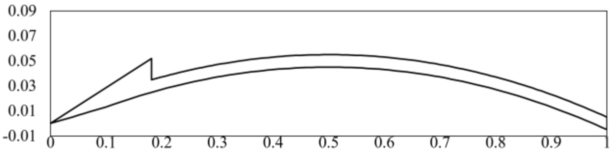

Figure 2 Arrow airfoil

The separation point is affected by the Reynolds number. Also, there is hysteresis in the unsteady operation process. Because of these points, it is difficult to predict the separation point and the performance. Therefore, by making the leading edge sharp to fix the separation point, the Reynolds number dependency and hysteresis can be solved. However, it is insufficient to maximize the effect of the bubble by increasing its size. Therefore, to increase the size of the bubble, a cliff shape is created on the top of the airfoil to increase the height and length of the bubble. The length of the cliff shape should be shortened, because the position of the cliff is too far back from the leading edge, the maximum length of the bubble is limited, and it is expected that an unpredictable flow will appear upstream of the cliff. The arrow shape is derived since the thin flat airfoil is combined with cliff shape, so it is named the arrow airfoil.

The flow characteristics due to the arrow shape are as follows. 1) The low-pressure region on the upper surface of the airfoil by separation bubble makes the lift increase. 2) Drag shows opposite aspects in pressure drag and friction drag. Although pressure drag increases due to low pressure caused by the bubble, the reverse flow inside the bubble makes friction drag decrease. At a low angle of attack, the pressure drag and friction drag have the same order of magnitude, so the effects of each other are canceled and the drag does not change much. At a high angle of attack, the pressure drag is larger than the friction drag, but the increment effect of pressure drag is not significant. As a result, 3) the L/D increases by the increase of the lift without the increase of the drag.

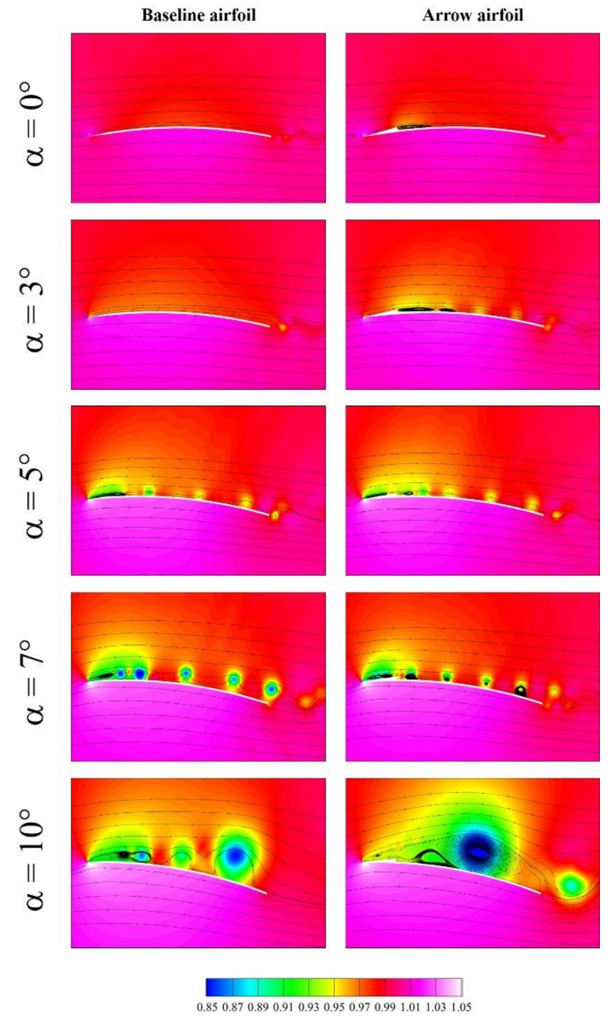

Figure 3 Pressure contour for baseline airfoil(left) and arrow airfoil(right)

Figure 3 shows the normalized pressure contour and streamline of the flow around each airfoil. In the case of baseline airfoil, a bubble is formed at the leading edge, LE bubble, at the angle of attack over 5°. In the case of the arrow airfoil, arrow bubble is formed from the angle of attack 0° due to the arrow shape. At the angle of attack 3°, the pressure inside the arrow bubble decreases, and as the size of the arrow bubble increases, vortex shedding occurs. At the angle of attack 5°, separation occurs at the leading edge like the baseline airfoil, and a LE bubble is generated. At the angle of attack 7°, vortex shedding occurs in the LE bubble, and this shedding interferes with the arrow bubble. Therefore the size of the bubble and the pressure do not decrease compared to the angle of attack 5°. However, in the case of baseline airfoil, the lower pressure region is formed due to vortex shedding. So the pressure of the upper surface of the baseline airfoil is lower than the arrow airfoil. At the angle of attack 10°, the vortex shedding of the arrow airfoil is strengthened, and the pressure decreases as the bubble bursts completely. To summarize, in the case of the baseline airfoil, the flow remains attached to the surface at a low angle of attack (less than 4°), but over 5°, separation occurs at the leading edge, and the LE bubble is formed. At the angle of attack over 7°, the bubble bursts, and the vortex shedding grows strong. In the case of arrow airfoil, the arrow bubble is formed from an angle of attack of 0°, and over 5°, LE bubble is formed. At the angle of attack 10°, the bubble bursts and vortex shedding becomes severe as the baseline airfoil.

Figure 4 (a) shows lift and drag coefficient of baseline airfoil and arrow airfoil according to the angle of attack. In both airfoils, there is almost no difference in lift and drag at an angle of attack less than 2°, but a difference occurs over 3°. In the case of an arrow airfoil, a non-linear increase of lift appeared at 3°, but the non-linear increase of lift is observed at 5° in the case of baseline airfoil. Since the nonlinear increase of lift occurs at lower angle of attack, arrow airfoil has higher lift than baseline airfoil at the angle of attack 3°. This is because, as shown in Figure 3, the size of the Arrow bubble increases, so the low pressure region of the arrow airfoil is larger than the baseline airfoil. At the baseline airfoil, the non-linearity of lift exists because the LE bubble is formed at the angle of attack 5°. At an angle of attack of 7°, lift of arrow airfoil is lower than baseline airfoil. Because the

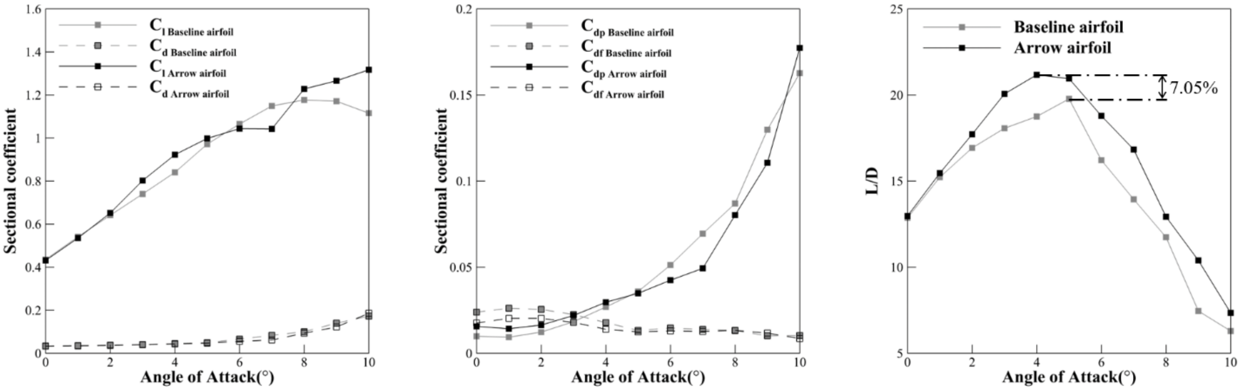

(a) (b) (c)

Figure 4 (a) Sectional coefficient; (b) Pressure and friction component of drag; and (c) L/D of the baseline airfoil and arrow airfoil

pressure of the upper surface of baseline airfoil is low due to the vortex shedding from the leading edge. In the case of the arrow airfoil, the interaction of LE bubble and Arrow bubble causes the size of the bubble to decrease. At the angle of attack 8°, the Arrow bubble also bursts, it can be seen that both lift and drag increase due to low pressure of upper surface. Figure 4 (b) shows the friction drag and pressure drag of both airfoils. Due to the low pressure region by the Arrow bubble, the pressure drag of the arrow airfoil is larger than the baseline airfoil at the low angle of attack. However, at the high angle of attack, the pressure drag of the arrow airfoil is lower than the baseline airfoil because bubble bursts in the baseline airfoil. In the case of the friction drag, because of the reverse flow in the bubble, the arrow airfoil has a lower friction drag than the baseline airfoil at the low angle of attack. At a low angle of attack, the high pressure drag of the arrow airfoil is offset by the low friction drag, and thus the drag of the arrow airfoil is almost the same as that of the baseline airfoil. At a high angle of attack, the bubble of both airfoils burst, so there is little difference in friction drag, and the pressure drag of arrow airfoil is smaller, so the drag of the arrow airfoil is smaller than the baseline airfoil. The lift of the arrow airfoil is higher than the baseline airfoil, but the drag of the arrow airfoil is the same as the baseline airfoil. As a result, shown in Figure 4 (c), the $\mathrm{L/D}$ of the arrow airfoil is higher than the baseline airfoil at all angle of attack.

3. METHODOLOGY

3.1. Numerical Analysis

3.1.1. Numerical Method

As a numerical analysis method, KFLOW[17], a structured grid-based solver of Konkuk University, is used. The unsteady, compressible Reynolds-averaged Navier-Stokes equation is used as the governing equation. For high-order accuracy, M-AUSMPW+[18] is used, and for accurate time advance, the second backward formula with dual time stepping is used, and for convergence, 20 calculations are performed per time step. Considering the low Reynolds flow, the $\mathrm{k}-\omega$ SST model is used with the $\gamma-\mathrm{Re}_{\theta}$ transition model.

Table 1 Operating conditions for Mars

Parameter	Earth	Mars
Density, $\rho(\mathrm{kg/m^3})$	1.225	1.67×10^{-2}
Temperature, $\mathrm{T(K)}$	288.8	248.2
Gas constant, $\mathrm{R}(\mathrm{m}^2/s^2 * K)$	287.1	188.9
Specific heat ratio, γ	1.4	1.289
Dynamic viscosity, $\mu(\times10^{-5}\mathrm{Ns/m^2})$	1.75	1.13
Static pressure, $\mathrm{p(kPa)}$	101.3	0.7
Sound speed, $\mathrm{c(m/s)}$	340.4	245.8

3.1.2. Flow Condition

Atmospheric conditions on Mars are different from those on Earth. The density of the atmosphere on Mars is about 1% of that of the Earth, and the temperature of the atmosphere is low. Although the air temperature differs by about 50K between day and night, the daytime temperature is used. Also, since it is a carbon dioxide-based atmosphere, the gas constant, specific heat ratio, and viscosity are different, and the pressure is also low. A comparison of atmospheric conditions on Earth and Mars is shown in Table 1. Operating flow conditions are calculated based on the blade planform of NASA's Mars Helicopter Technology Demonstrator (MHTD)[19]. Figure 5 shows the blade planform of MHTD. The diameter of the blade is 1.2m and the RPM is 2390 at hovering. Numerical analysis and optimization are performed under flow conditions at $r = 0.3, r = 0.5,$ and $r = 0.9$ (station 1, station 2, station 3, respectively) in the spanwise direction. Table 2 shows the flow conditions for each spanwise position.

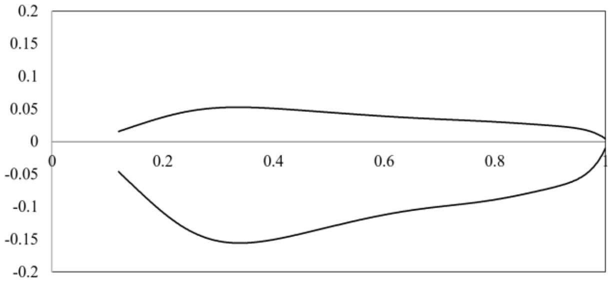

Figure 5 Blade planform of Mars Helicopter Technology Demonstrator

Table 2 Flow conditions of each spanwise location

Non-dimensional spanwise Location (r)	Reynolds number	Mach number
0.3(station 1)	8,298	0.1869
0.5(station 2)	11,912	0.3116
0.9(station 3)	11,711	0.5608

3.1.3. Computational Domain

The computational domain is shown in Figure 6. It is a square structured grid, and the distance from the airfoil to the far-field is 50 chord length. Grid convergence test is performed based on the baseline airfoil, and the results are shown in Figure 7. As a result of the grid convergence test, the grid which has 40,000 cells and 0.1 of $y+$ is used. 300 points are assigned in the chord direction on the baseline airfoil, and 50 points are assigned to the far-field from the airfoil. In the case of arrow airfoil, there is a slight difference depending on the number of points according to the difference in arrow shape.

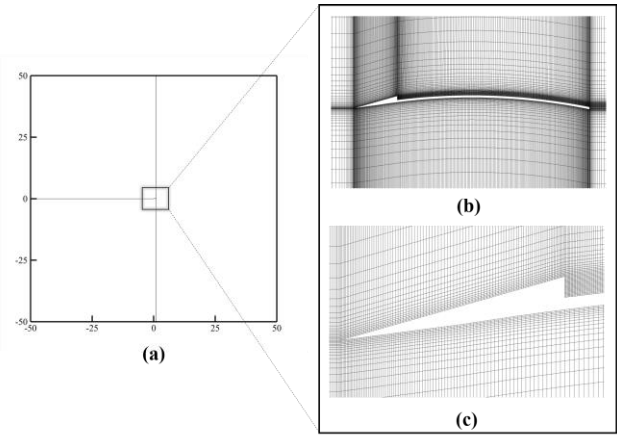

Figure 6 (a) Square structured computational domain; (b) frid around airfoil; and (c) grid around arrow

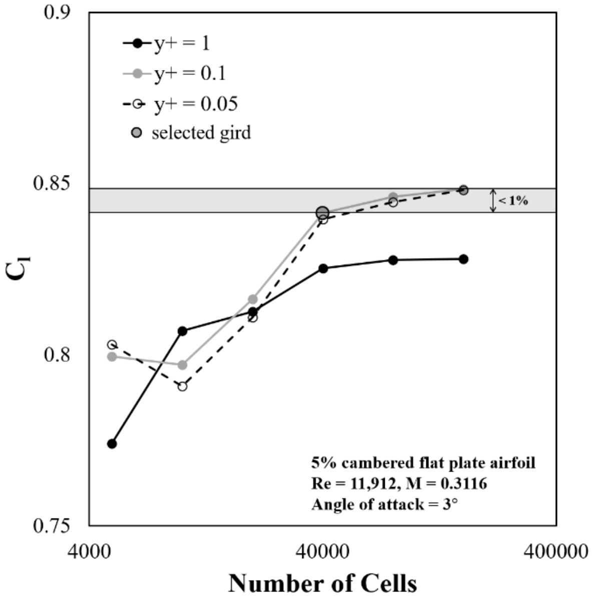

Figure 7 Convergence test of grid resolution of baseline airfoil at angle of attack 3°

3.1.4. Validation

To validate the numerical analysis method and turbulence model, the experimental results of Munday[4] and the numerical results of Koning[14] are compared. The triangular airfoil which maximum thickness is 5% of the chord length, and located at 30% chord length from the leading edge is used in the experiment. The flow conditions are $\mathrm{Re} = 3{,}000, \mathrm{M} = 0.15$. In the numerical analysis by Koning, OVERFLOW is used, and Spalart-Allmaras (SA) 1- equation turbulence model (SA-neg-1a) with the Coder 2-equation Amplification Factor Transport (AFT) transition model (SA-AFT2017b) is used. It is an unsteady calculation, and the 6th order central difference method and 2nd order BDF2 time advance are used.[14]

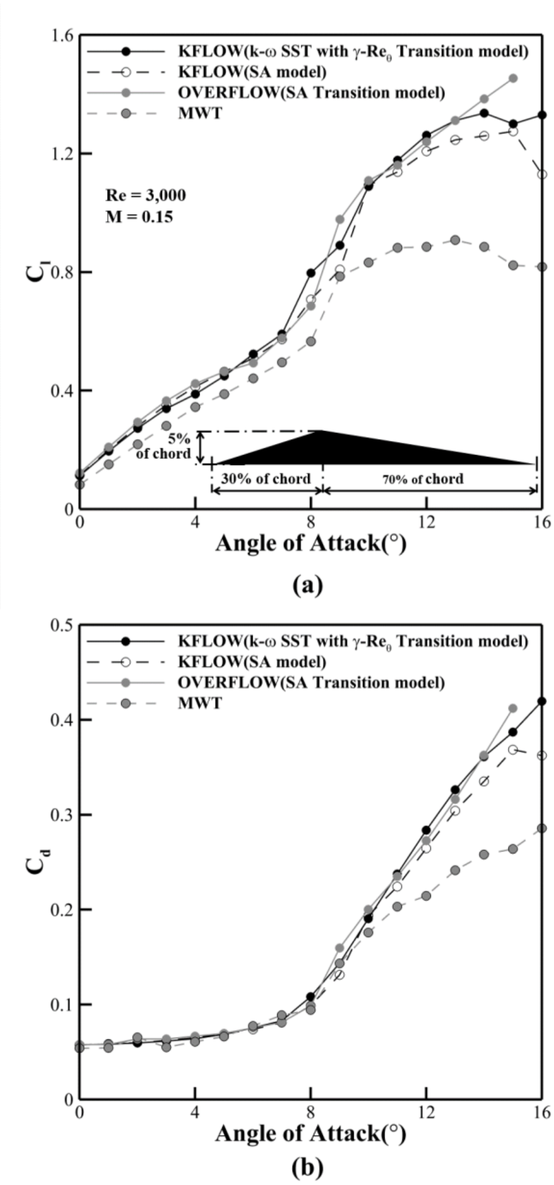

Figure 8 Comparison of sectional (a) lift; and (b) drag coefficients at $Re = 3{,}000$ and $M = 0.15$ for triangular airfoil from the present work using KFLOW and experimental results from Munday et al[4], and numerical analysis(Spalart Almaras with transition model) from Koning[14]

Figure 8 shows comparing lift and drag coefficient for each turbulence model with Munday's experimental results and Koning's numerical results. The non-linearity of lift at the angle of attack 8° is shown in Munday's results. The results from Koning also show the non-linearity of lift at the angle of attack 8°, but it overestimates. In addition, the lift of experimental results decreases at the angle of attack 12°, but OVERFLOW does not follow it. In the case of KFLOW, the Spalart-Allmaras model shows the non-linearity of lift at the angle of attack 9°, but it does not fit well with the results of OVERFLOW and does not follow the trend of the experimental results. The $\mathrm{k}-\omega$ SST turbulence model and the $\gamma-\mathrm{Re}_\theta$ transition model not only simulates non-linearity of lift well but also predicts lift reduction at the high angle of attack. Therefore, in this paper, the $\mathrm{k}-\omega$ SST turbulence model is used together with the $\gamma-\mathrm{Re}_\theta$ transition model.

3.2. Definition of Design Problem

3.2.1. Design Objective Functions

The objective function is the maximum $\mathrm{L/D}$ in the range of the angle of attack 0~10°. In addition, in consideration of the robustness of the rotor operating conditions and pitch angle, the constraint is set that the $\mathrm{L/D}$ is larger than that of the baseline airfoil within all angle of attack ranges.

3.2.2. Design Variables and Sampling

An arrow airfoil is created by adding an arrow shape based on a 5% cambered flat plate airfoil. The arrow shape is parameterized by the length of the arrow shape, the distance from the leading edge to the cliff shape, and the angle from the chord line. As design constraints, the thickness of the airfoil including the arrow shape should not exceed 5% of the chord length. Two design variables are used, and 30 airfoils are sampled through the Latin Hypercube Sampling method to make a surrogate model. Figure 9 shows the parameterization method of the arrow and the selected design variables in the design space. The shaded region indicates the area not satisfying the constraint. The sampled arrow airfoils are shown in Figure 10.

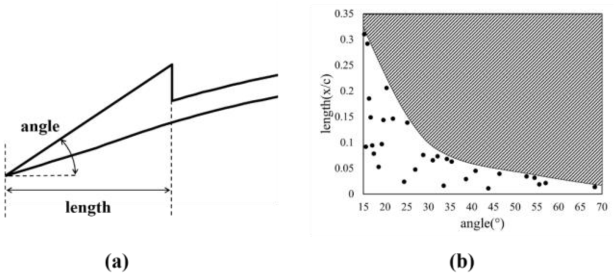

Figure 9 (a) Design variables of arrow shape; and (b) selected design variables sets by Latin Hypercube Sampling and shaded area represent that doesn't meet the constraints

3.2.3. Surrogate Model & Optimization

Lift and drag coefficient are calculated through numerical analysis of the sampled airfoil under the three flow conditions in Table 2. The maximum $\mathrm{L/D}$ according to each design variable is also derived. Based on the calculated aerodynamic coefficient, a surrogate model is created using Elliptical Basis Function approximation. And the validity is verified through cross validation[20]. Figure 11 shows the cross validation results. When comparing the actual and predicted values for lift and drag under three flow

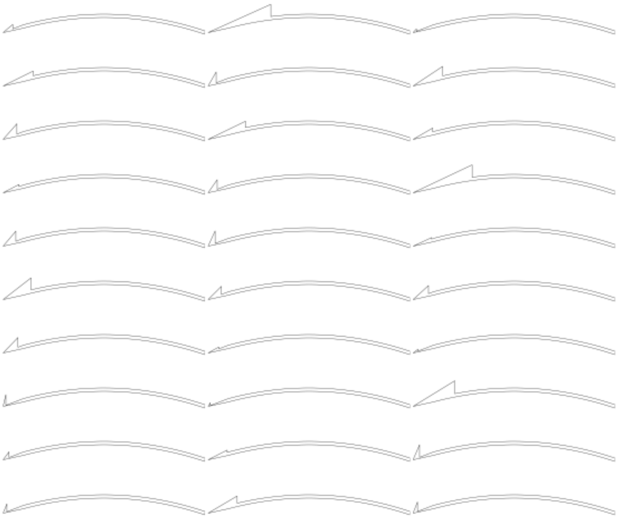

Figure 10 Sampled arrow airfoils

conditions, all R^2 values are 0.95 or higher, confirming that the surrogate model is well generated. Figure 12 is the generated surrogate model, which is the maximum L/D according to each design variable. In Station 1, the optimum design will be located at the arrow angle is about 20° and the arrow length is 0.13. In Station 2, the optimum design will be located at the arrow angle is about 18° and the arrow length is 0.18. In Station 3, the arrow with an arrow angle of about 55° and an arrow length of 0.01 shows the maximum L/D. The arrow is optimized based on the generated surrogate model to maximize the maximum L/D. A genetic algorithm is used as the optimization method, and a total of 1000 factors were processed for 100 generations.

4. RESULTS

4.1. Optimization Results

Figure 13 shows the optimized arrow airfoil in Station 1 and performance comparison with the baseline airfoil. The optimized arrow has a length of 0.1853 of the chord length and the arrow angle is 16.41°.

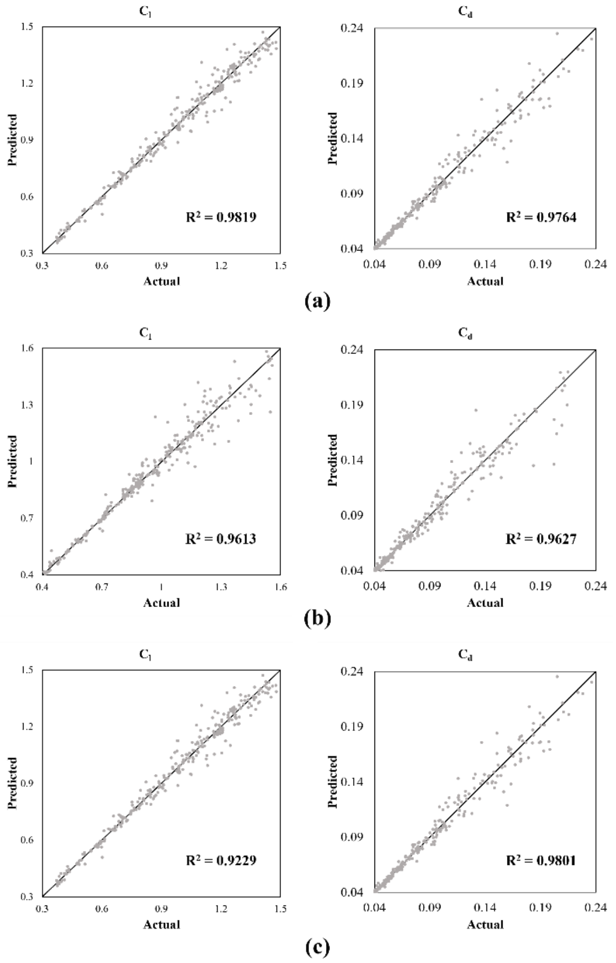

Figure 11 Maximum L/D contour from surrogate model at (a) station 1; (b) station 2; and (c) station 3

Figure 13 (a) compares the L/D of each airfoil according to the angle of attack. At the angle of attack 4°, the L/D of the arrow airfoil is significantly larger than the L/D of the baseline airfoil, and the maximum L/D increases 10.51%. Figure 13 (b) compares lift and drag of each airfoil. In the case of the baseline airfoil, lift increases linearly, but in arrow airfoil, the non-linear increase in lift occurs at the

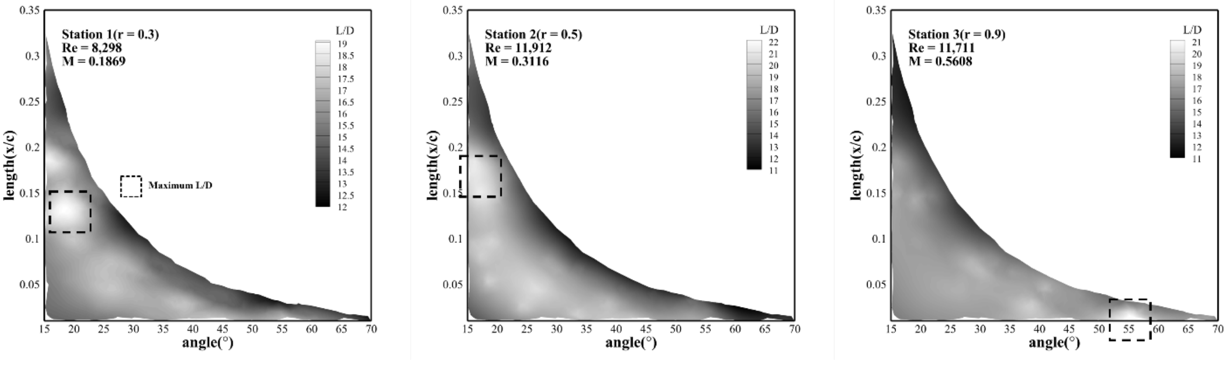

(a) (b) (c)

Figure 12 Maximum L/D contour from surrogate model at (a) station 1; (b) station 2; and (c) station 3

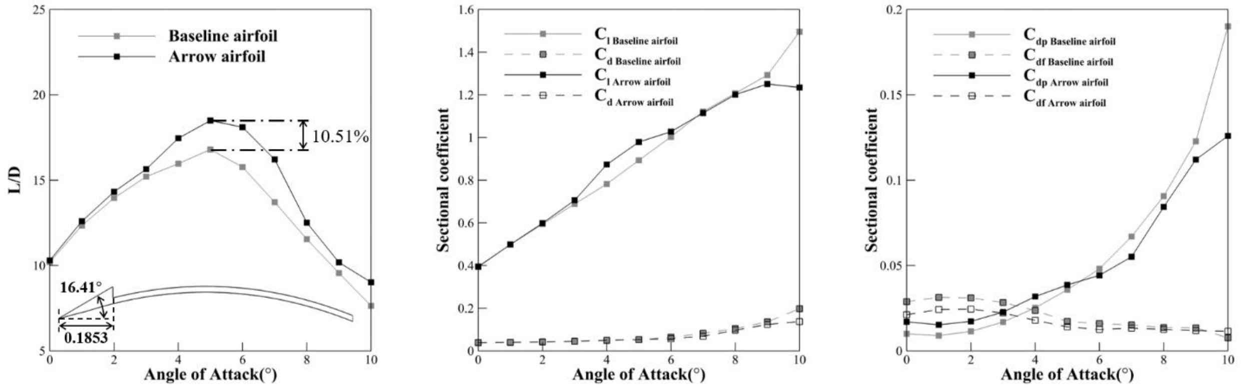

(a) (b) (c)

Figure 13 (a) Geometry of optimized arrow airfoil and L/D compare with baseline airfoil at station 1; (b) compare of sectional coefficient of airfoils corresponding to angle of attack; and (c) compare of pressure and friction drag of airfoils corresponding to angle of attack

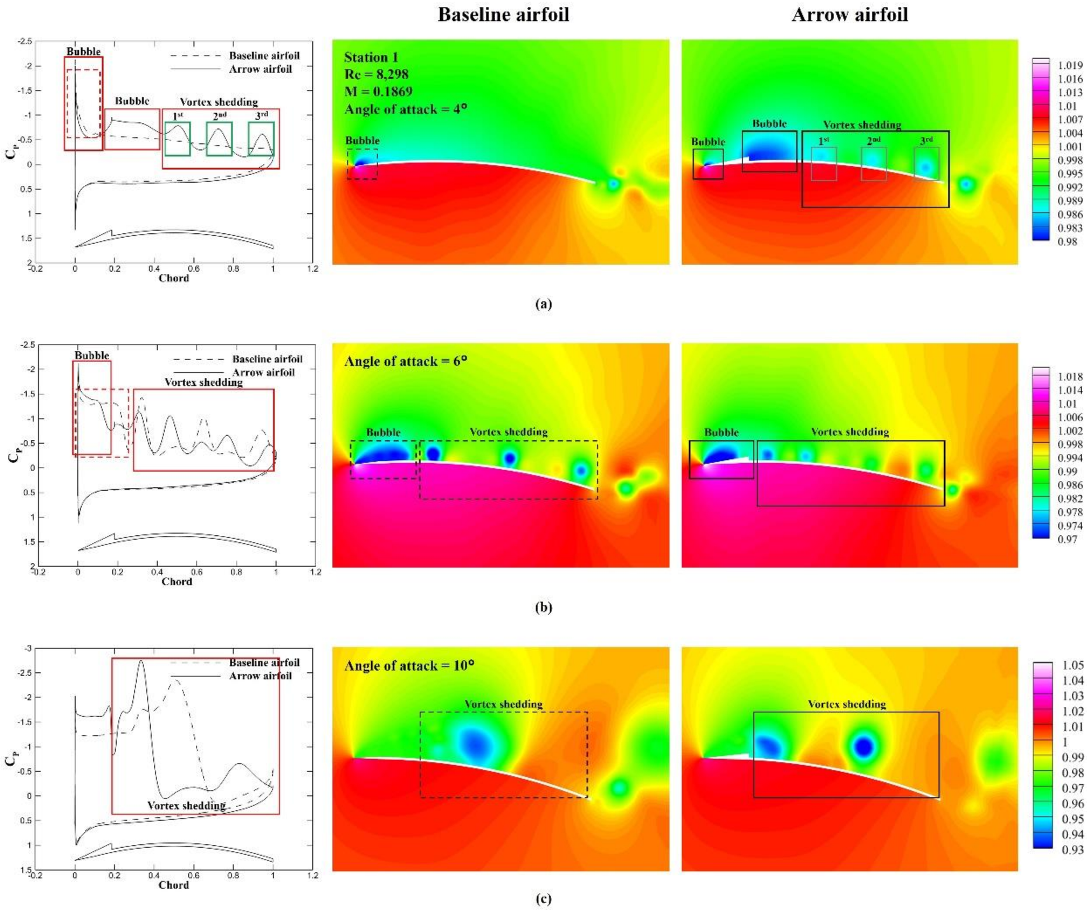

Figure 14 Compare of C_P and pressure contour of baseline and arrow airfoils at (a) angle of attack 4°; (b) angle of attack 6°; and (c) angle of attack 10°

angle of attack 4°. And at the angle of attack 6°, the gradient of lift decreases, and after the angle of attack 9°, lift starts to decrease. In baseline airfoil, lift increases linearly and lift increase drastically after the angle of attack of 9°, but drag also increase drastically, too. So at the angle of attack lower than 7°, lift of the arrow airfoil is larger than that of the baseline airfoil, and there is little difference in drag. The angle of attack higher than 8°, lift of the baseline airfoil is larger, but drag is also larger. Figure 13 (c) shows drag of each airfoil divided into pressure drag component and friction drag component. Friction drag of the arrow airfoil is smaller than the baseline airfoil at all angle of attack except 10°, and pressure drag of the arrow airfoil is larger than the baseline airfoil at the angle of attack less than 5°, but it is smaller than the baseline airfoil at the higher angle of attack. So at the angle of attack less than 5°, the total drag of the baseline airfoil and the arrow airfoil is similar, and higher than 5°, because of smaller pressure drag, drag of the arrow airfoil is smaller than the baseline airfoil.

Figure 14 shows the $\mathrm{C_P}$ graph and the normalized pressure contour of each airfoil at station 1. Figure 14 (a) is about the angle of attack 4°. The bubble formed only at the leading edge in the baseline airfoil, but the arrow bubble and the vortex shedding occurs in the arrow airfoil. It can be seen that both airfoils have almost the same $\mathrm{C_P}$ around the leading edge, but downstream, $\mathrm{C_P}$ of the arrow airfoil is lower than the baseline airfoil due to vortex shedding. This $\mathrm{C_P}$ difference makes the arrow airfoil has a larger lift and pressure drag than the baseline airfoil at a low angle of attack. Figure 14 (b) is about the angle of attack 6°. The LE bubble of the baseline airfoil becomes larger than the bubble at 4°, and vortex shedding occurs. In the case of arrow airfoil, the LE bubble occurs, and the vortex shedding from LE bubble interference with the arrow bubble. So the size of the arrow bubble can't grow large, lift increase rate decreases as seen in Fig. 13 (b). Figure 14 (c) is about the angle of attack 10°. At the angle of attack 10°, a stall occurs in both airfoils resulting in large vortex shedding. Around the leading edge, the arrow airfoil has a lower pressure than the baseline airfoil, and around the trailing edge, the baseline airfoil has a lower pressure than the arrow airfoil. Because of the geometry property of circular arc airfoil, low pressure at the trailing edge causes large pressure drag. So baseline airfoil has a larger drag than arrow airfoil.

Figure 15 shows the optimized arrow airfoil in Station 2 and performance comparison with the baseline airfoil. The optimized arrow airfoil has an arrow length of 0.1817 of the chord length and an arrow angle of 15.91°, which is almost the same as the optimized arrow shape in station 1, but both arrow length and angle are smaller than in station 1. Figure 15 (a) compares the $\mathrm{L/D}$ of each airfoil at the angle of attack. At the angle of attack 2°, $\mathrm{L/D}$ of the arrow airfoil starts to significantly increase than the $\mathrm{L/D}$ of the baseline airfoil, and the maximum $\mathrm{L/D}$ increases 10.51% at the angle of attack 4°. Unlike station 1, in the case of baseline airfoil, lift nonlinearly increases at an angle of attack 5°, but starts to decrease at an angle of attack 8°. In the case of the arrow airfoil, lift nonlinearly increases at an angle of attack 3°, and the increase rate of lift decreases at an angle of attack of 5°, and decreases at an angle of attack of 7°. However, it can be seen that lift increases again at an angle of attack beyond that. In the case of drag, it has the same trend as that of station 1, and there is little difference in drag at low angle of attack, and it can be confirmed that drag of arrow airfoil is smaller than baseline at high angle of attack. Figure 15 (c) shows drag of each airfoil divided into pressure drag component and friction drag component. Like station 1, friction drag of the arrow airfoil is smaller than the baseline airfoil at all angle of attack, and in pressure drag, it has a low angle of attack, less than 4°. Pressure drag of the arrow airfoil is larger than the baseline airfoil at the angle of attack less than 4°, but it is smaller than the baseline airfoil at the higher angle of attack except 10°.

Figure 16 shows the $\mathrm{C_P}$ graph and the normalized pressure contour of each airfoil at station 2. Figure 16 (a) is about the angle of attack 3°. In the baseline airfoil, the bubble doesn't form, but the arrow bubble and the vortex shedding occurs in the arrow airfoil. This makes $\mathrm{C_P}$ difference, and the arrow airfoil has a larger lift and pressure drag than the baseline airfoil at a low angle of attack. Figure 15 (b) is about the angle of attack 5°. The LE bubble is formed at the baseline airfoil, causing a nonlinear lift increase. In the case of arrow airfoil, the LE bubble occurs and the vortex shedding interference with the arrow bubble. So it shows a similar $\mathrm{C_P}$ distribution in the baseline airfoil and arrow airfoil. Figure 16 (c) is about the angle of attack 7°. The size of the bubble in baseline airfoil doesn't increase compared with the angle of attack 5°, but the vortex shedding becomes stronger. In the case of the arrow airfoil, the pressure in the leading edge is lower than the baseline airfoil, but vortex shedding is weak than the baseline airfoil. Figure 16 (d) is about the angle of attack 10°. A stall occurs in both airfoils resulting in large vortex shedding. Contrary to station 1, since the pressure difference in the arrow airfoil is larger than the baseline airfoil and the low pressure region is located at the trailing edge, the lift and drag of the arrow airfoil are larger than those of the baseline airfoil.

In station 3, no optimized arrow airfoil is derived. This is because the constraint, the $\mathrm{L/D}$ of the optimized arrow airfoil should be larger than that of the baseline airfoil, doesn't be met. The only difference in the condition of the flow between station 2 and 3 is the Mach number. Therefore, to investigate the effect of Mach number, numerical analysis is performed at various Mach numbers at fixed $\mathrm{Re} = 11{,}912$.

4.2. Mach Number Efffects

To investigate the effects of the Mach number on the performance of the arrow airfoil, off-design is conducted at various Mach number in the range of the angle of attack 0~10°. The arrow airfoil optimized in station 2 is used.

Figure 17 shows $\mathrm{L/D}$, lift and drag coefficient according to the angle of attack for each Mach number of arrow airfoil optimized in station 2. There

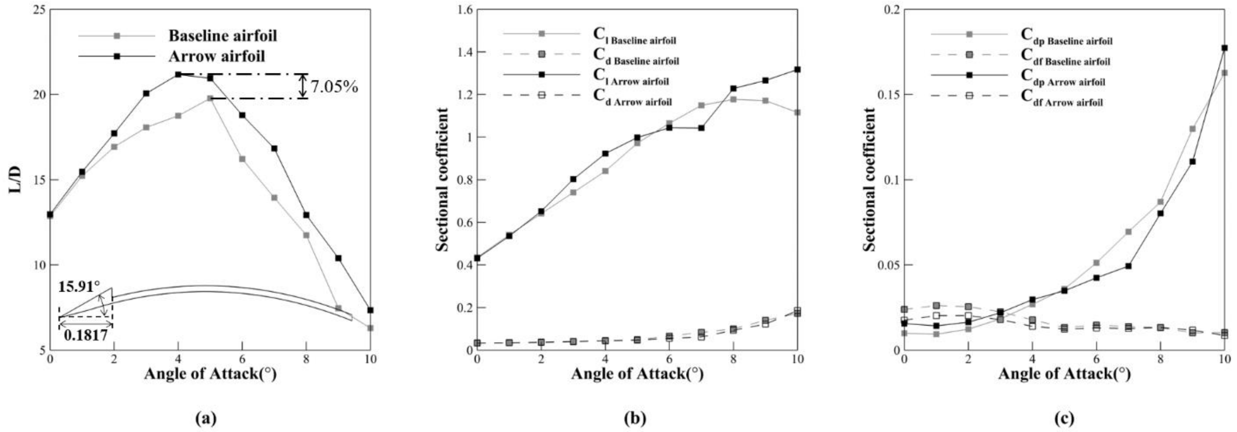

Figure 15 (a) Geometry of optimized arrow airfoil and L/D compare with baseline airfoil at station 2; (b) compare of sectional coefficient of airfoils corresponding to angle of attack; and (c) compare of pressure and friction drag of airfoils corresponding to angle of attack

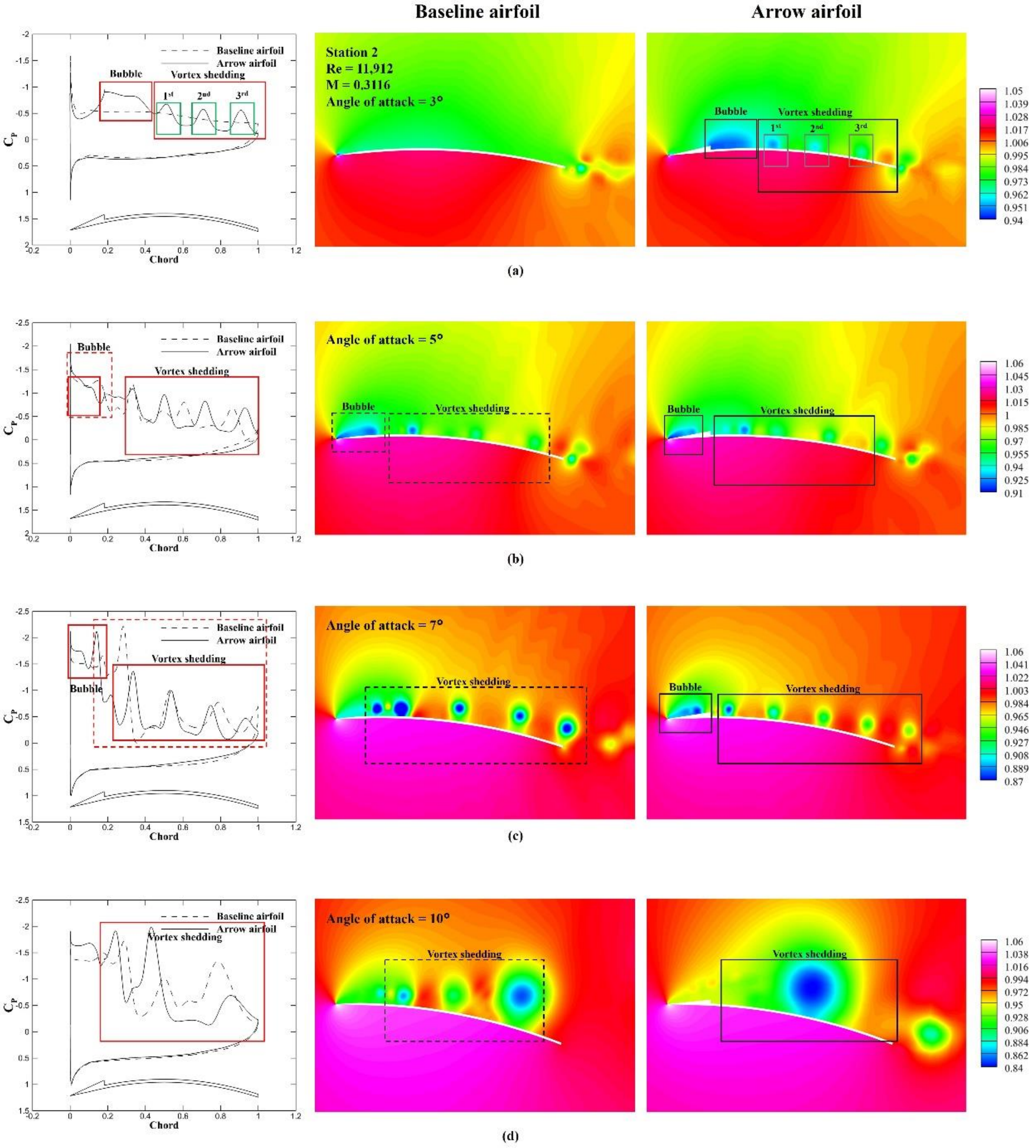

Figure 16 Compare of C_P and pressure contour of baseline and arrow airfoils at (a) angle of attack 3°; (b) angle of attack 5°; (c) angle of attack 7° and (d) angle of attack 10°

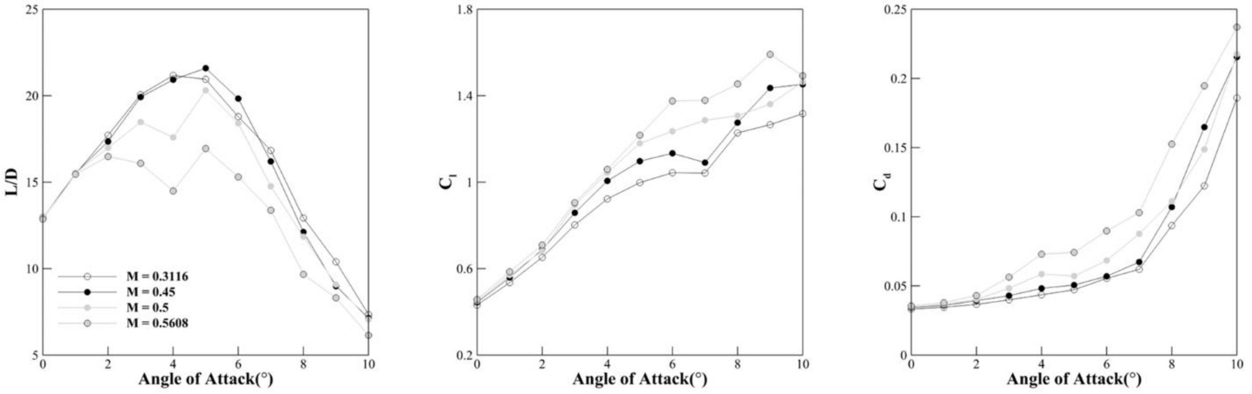

Figure 17 (a) L/D compare by Mach number; (b) compare of sectional lift coefficient by Mach number corresponding to angle of attack; and (c) compare of sectional drag coefficient by Mach number corresponding to angle of attack

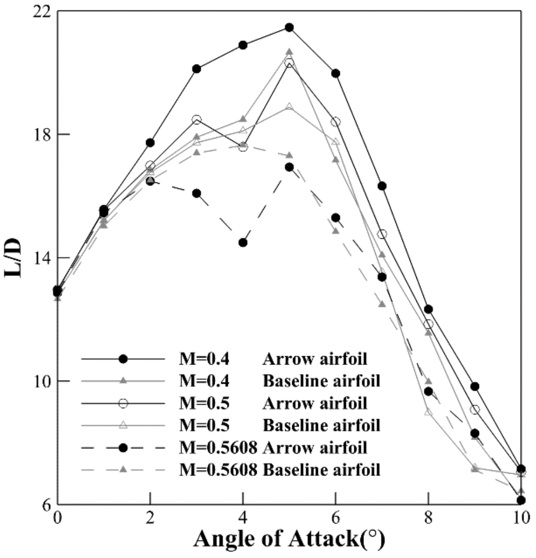

Figure 18 Compare of L/D of baseline airfoil and arrow airfoil by Mach number

is no significant change between $\mathrm{M} = 0.3116$ (Station 2) ~ 0.45, so only $\mathrm{M} = 0.3116$ and $\mathrm{M} = 0.45$ are displayed. At $\mathrm{M} = 0.5$, $\mathrm{L/D}$ decreases remarkably. Both $\mathrm{M} = 0.5$ and $\mathrm{M} = 0.5608$ show two maxima, which increase from 0° to 4° at the angle of attack and then decrease, and increase again from the angle of attack above 5°. This is due to the sharp increase in drag at the angle of attack 4°. When $\mathrm{M} = 0.5$ and $\mathrm{M} = 0.5608$, drag continues to increase up to an angle of attack 4°, but the drag at an angle of attack 4° and 5° is almost the same. In the case of lift, after the nonlinear increase occurs at the angle of attack 3°, lift also increases as the angle of attack increases, so two maxima appear as described above.

Figure 18 shows $\mathrm{L/D}$ according to the angle of attack of the baseline airfoil and the arrow airfoil when $\mathrm{M} = 0.4$, $\mathrm{M} = 0.5$, and $\mathrm{M} = 0.5608$. Until $\mathrm{M} = 0.4$, the $\mathrm{L/D}$ of the arrow airfoil is larger than that of the baseline airfoil at all angle of attack, but from $\mathrm{M} = 0.5$ and above, the $\mathrm{L/D}$ of the baseline airfoil is larger due to the increase in drag of the arrow airfoil at the angle of attack 4°. The reason that the sharp increase of drag of the arrow airfoil above $\mathrm{M} = 0.5$ is shown in Figure 19. Figure 19 shows $\mathrm{C_P}$ and normalized pressure contour graph from $\mathrm{M} = 0.3116$ to $\mathrm{M} = 0.5608$ of arrow airfoil. There is no difference between each Mach number at an angle of attack 2° in figure 19 (a). However, a large difference occurs at the trailing edge at the angle of attack 4° in Fig. 19 (b). The intensity of the vortex shedding increases with Mach number, i.e velocity of flow. As mentioned above, the low pressure around the trailing edge causes drag to increase. For this reason, $\mathrm{L/D}$ decreases at an angle of attack of 4° from $\mathrm{M} = 0.5$ or higher.

5. CONCLUSIONS

In this study, a novel arrow airfoil is proposed in the Mars atmospheric condition for high $\mathrm{L/D}$, and the flow characteristics around the airfoil are investigated through numerical analysis. By applying the newly proposed arrow shape to 5% cambered flat plate airfoil, it is confirmed that the arrow shape affects the bubble generation and increases $\mathrm{L/D}$. The low pressure region on the upper surface of the airfoil by arrow bubble makes the lift increase. Although pressure drag increases due to low pressure inside the bubble, the reverse flow inside the bubble makes friction drag decrease. As a result, $\mathrm{L/D}$ increases by the increase of the lift without the increase of the drag.

The arrow airfoils are optimized under 3 flow conditions based on 3 blade spanwise locations of the NASA MHTD. The objective function is the maximum $\mathrm{L/D}$ in range of angle of attack 0 to 10° . And the constraint is that $\mathrm{L/D}$ of the arrow airfoil should larger than baseline in all angle of attack. As a results, the maximum $\mathrm{L/D}$ increases by 10.51%

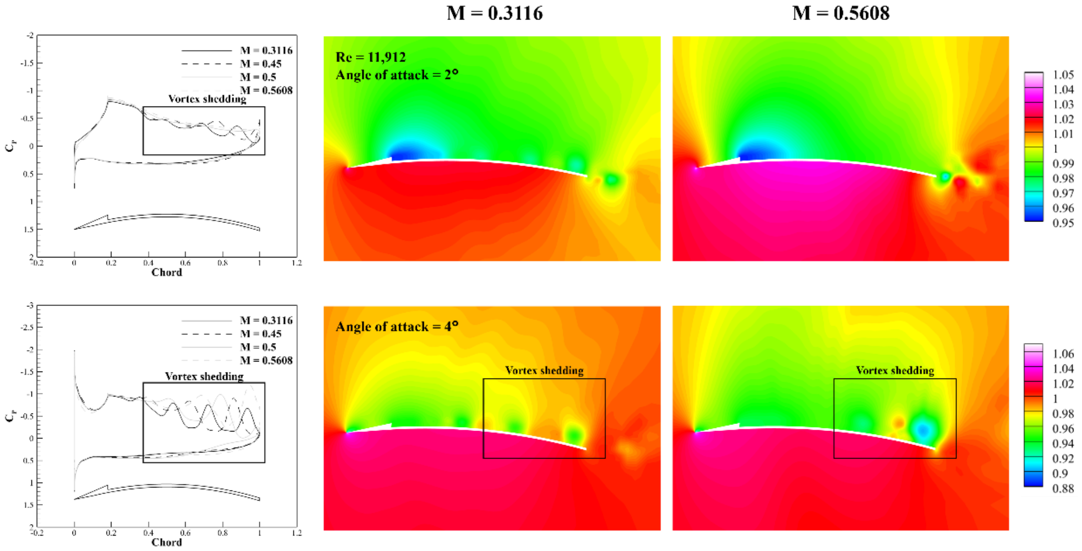

Figure 19 Compare of C_P and pressure contour by Mach number at (a) angle of attack 2°; and (b) angle of attack 4°

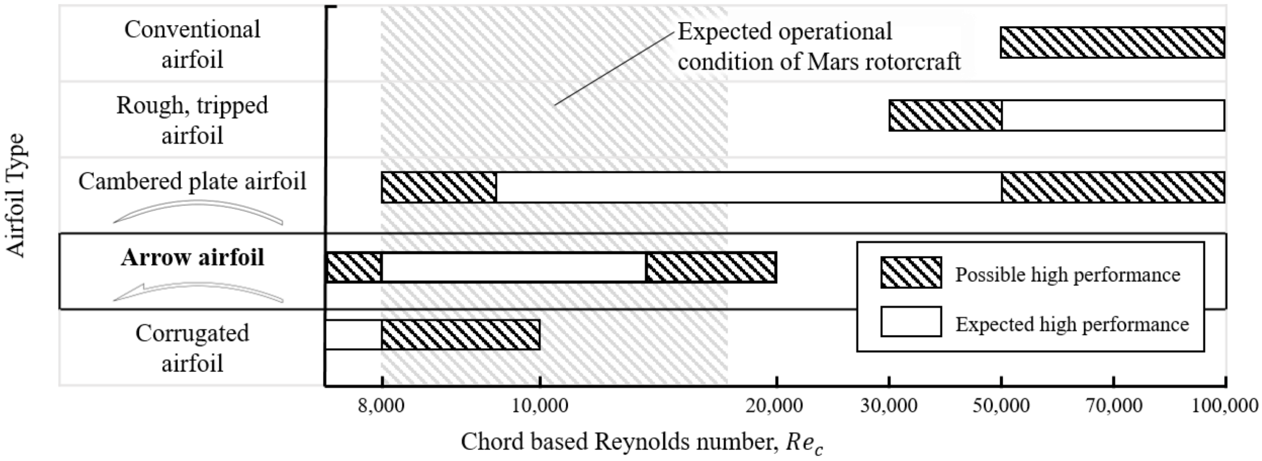

Figure 20 Performance of each type of airfoil in operational condition of Mars rotorcraft

and 7.05% in stations 1 and 2, respectively, and the result that satisfies the constraint is not derived in station 3.

Off-design study is conducted to investigate the effect of the Mach number based on the Reynolds number of the flow condition at station 2. The higher Mach numbers, the length of the bubble increases, the vortex shedding gets stronger before generating sufficient lift. As the vortex shedding becomes stronger, the low pressure region is formed at trailing edge. It makes the drag increase drastically, and L/D decreases than the baseline. At M = 0.5 or less, arrow airfoil has higher L/D than baseline airfoil in all angle of attack, but performance is inferior thereafter.

Through the present optimization study of the arrow airfoil, the new type of the airfoil is proposed which is expected to show high performance in the present operational conditions of Mars rotorcraft.

REFERENCES

[1] Arena, A. V., and Mueller, T. J. "Laminar Separation, Transition, and Turbulent Reattachment near the Leading Edge of Airfoils." *AIAA Journal*, Vol. 18, No. 7, 1980, pp. 747–753. https://doi.org/10.2514/3.50815.

[2] O'meara, M. M., and Mueller, T. J. "Laminar Separation Bubble Characteristics on an Airfoil at Low Reynolds Numbers." *AIAA Journal*, Vol. 25, No. 8, 1987, pp. 1033–1041. https://doi.org/10.2514/3.9739.

[3] Sunada, S., Ozaki, K., Tanaka, M., Yasuda, T., Yasuda, K., and Kawachi, K. "Airfoil Characteristics at a Low Reynolds Number." *Journal of Flow Visualization and Image Processing*, Vol. 7, No. 3, 2000, pp. 207–215.

https://doi.org/10.1615/jflowvisimageproc.v7.i3.20.

[4] Munday, P. M., Taira, K., Suwa, T., Numata, D., and Asai, K. "Nonlinear Lift on a Triangular Airfoil in Low-Reynolds-Number Compressible Flow." *Journal of Aircraft*, Vol. 52, No. 3, 2015, pp. 924–931. https://doi.org/10.2514/1.C032983.

[5] Lee, D. H., Nonomura, T., Oyama, A., and Fujii, K. "Comparison of Numerical Methods Evaluating Airfoil Aerodynamic Characteristics at Low Reynolds Number." *Journal of Aircraft*, Vol. 52, No. 1, 2015, pp. 296–306. https://doi.org/10.2514/1.C032721.

[6] Lee, D., Nonomura, T., Oyama, A., and Fujii, K. "Comparative Studies of Numerical Methods for Evaluating Aerodynamic Characteristics of Two-Dimensional Airfoil at Low Reynolds Numbers." *International Journal of Computational Fluid Dynamics*, Vol. 31, No. 1, 2017, pp. 57–67. https://doi.org/10.1080/10618562.2016.1274398.

[7] Schmitz, F., "Aerodynamics of the model airplane. Part 1. Airfoil measurements. Translated from German by Translation Branch, Redstone Scientific Information Center," Research and Development Directorate, United States Army Missile Command, Redstone Arsenal, Alabama, Vol. 35809, 1967.

[8] Schmitz, F., "The Aerodynamics of Small Reynolds Numbers," NASA Technical Memorandum, 1980.

[9] LIEBECK, R., "Laminar separation bubbles and airfoil design at low Reynolds numbers," *10th Applied Aerodynamics Conference*, 1992, pp. 441–456, doi: 10.2514/6.1992-2735.

[10] Oyama. A., and Fujii, K., "A study on airfoil design for future Mars airplane," *Collection of Technical Papers - 44th AIAA Aerospace Sciences Meeting*, 2006, vol. 23, no. January, doi: 10.2514/6.2006-1484.

[11] Tanaka, Y., Okabe, Y., Suzuki, H., Nakamura, K., Kubo, D., Tokuhiro, M., and Rinoie, K., "Conceptual Design of Mars Airplane for Geographical Exploration," Proceedings of the 36th JSASS Annual Meeting, JSASS, Tokyo, 2005, pp. 61-64

[12] Zhao, P., Quan, Q., Chen, S., Yang, T., Bai, D., Tang, D., and Deng, Z. "Geometry Shape Selection of NACA Airfoils for Mars Rotorcraft." *Acta Astronautica*, Vol. 157, No. December 2018, 2019, pp. 300–309. https://doi.org/10.1016/j.actaastro.2018.12.026.

[13] Koning, W. J. F., Romander, E. A., and Johnson, W. Low Reynolds Number Airfoil Evaluation for the Mars Helicopter Rotor. No. 2018-May, 2018, pp. 1–17.

[14] Koning, W. J. F., Romander, E. A., and Johnson, W. Performance Optimization of Plate Airfoils for Martian Rotor Applications Using a Genetic Algorithm. 2019.

[15] Koning, W. J. F. "*Airfoil Selection for Mars Rotor Applications,"* 2019.

[16] Koning, W. J. F. "Optimization of Low Reynolds Number Airfoils for Martian Rotor Applications Using an Evolutionary Algorithm." *AIAA Scitech 2020 Forum*, No. 0084, 2020, pp. 1–28. https://doi.org/10.2514/6.2020-0084.

[17] Kim, J. W., Park, S. H., and Yu, Y. H. "Euler and Navier-Stokes Simulations of Helicopter Rotor Blade in Forward Flight Using an Overlapped Grid Solver." *19th AIAA Computational Fluid Dynamics Conference*, No. June, 2009, pp. 1–13. https://doi.org/10.2514/6.2009-4268.

[18] Kim, K. H., and Kim, C. "Accurate, Efficient and Monotonic Numerical Methods for Multi-Dimensional Compressible Flows. Part I: Spatial Discretization." *Journal of Computational Physics*, Vol. 208, No. 2, 2005, pp. 527–569. https://doi.org/10.1016/j.jcp.2005.02.021.

[19] Bob Balaram, J., Canham, T., Duncan, C., Golombek, M., Grip, H. F., Johnson, W., Maki, J., Quon, A., Stern, R., and Zhu, D. "Mars Helicopter Technology Demonstrator." *AIAA Atmospheric Flight Mechanics Conference, 2018*, No. 209999, 2018, pp. 1–18. https://doi.org/10.2514/6.2018-0023.

[20] Jones, D. R., Schonlau, M., and W. J. Welch. "Efficient Global Optimization of Expensive Black-Box Functions." *Journal of Global Optimization*, Vol. 13, 1998, pp. 455–492.